IEEE Access
Multidisciplinary | Rapid Review | Open Access Journal

Received 16 June 2022, accepted 17 July 2022, date of publication 8 August 2022, date of current version 24 August 2022.

Digital Object Identifier 10.1109/ACCESS.2022.3197586

TOPICAL REVIEW

Comprehensive Evaluation of Magnetic Particle Imaging (MPI) Scanners for Biomedical Applications

MUHAMMAD IRFAN[1,2], (Member, IEEE), AND NURCAN DOGAN[2]
[1]Department of Electronics Engineering, Gebze Technical University, 41400 Gebze, Kocaeli, Türkiye
[2]Department of Physics, Gebze Technical University, 41400 Gebze, Kocaeli, Türkiye

Corresponding authors: Muhammad Irfan (mirfans1990@gmail.com) and Nurcan Dogan (nurcandogan80@gmail.com)

This work was supported by the Scientific and Technological Research Council of Türkiye (TUBITAK) under Grant 115E776.

ABSTRACT Magnetic particle imaging (MPI) is an emerging tomographic imaging technique that tracks and quantitatively measures the spatial distribution of the superparamagnetic iron oxide nanoparticles (SPIONs). It is a radiation-free, background-free, and signal attenuation-free imaging modality that utilizes the non-linear behavior of the tracer agents. The minimum acquisition time, high spatial resolution, and extreme sensitivity make it ideal for medical imaging in comparison to magnetic resonance imaging (MRI), computed tomography (CT), and positron emission tomography (PET). SPIONs are the main source of signal generation and have a significant influence on MPI scanner characteristics. Many research groups in the world are working to produce optimal tracer agents with a low toxicity profile for MPI applications. Versatile MPI scanners are developed and implemented at the pre-clinical stage to evaluate the performance of the system parameters. This review aims at giving an overview of the current developments and significant achievements of the tracer agents, imager design, image reconstruction, and potential applications of MPI scanners since their first exposure to the scientific world in 2005.

INDEX TERMS Computed tomography (CT), magnetic particle imaging (MPI), magnetic resonance imaging (MRI), positron emission tomography (PET), superparamagnetic iron oxide nanoparticles (SPIONs).

I. INTRODUCTION

Magnetic particle imaging (MPI) is a distinctive tomographic technique invented by Bernhard Gleich in 2001 at Philips Research Laboratory, Hamburg. A single-dimensional (1D) proof of concept device was initially presented in 2005 by Gleich and Weizenecker to the scientific world [1]. Gleich *et al.* extended the MPI scanner in 2008 to scan a 2D scanning area of 1×1 cm^2 with a Lissajous scanning sequence at 25 frames per second [2]. The hardware of the MPI imager was modified to a 3D level in 2009 for real-time acquisition (in vivo). The movement of the bolus through the cardiovascular system of the healthy mouse was recorded with a high temporal resolution of 21 ms for 4D imaging [3].

The useful imaging space of the MPI scanners in the middle of the geometry is commonly defined as bore size (diameter) which is used for phantoms, in vivo/in vitro small animals, and patients. The bore size of the initially presented scanners was just 32 mm. Moreover, continued research on the hardware modification yielded a 12 cm bore size, and scanning of large spaces becomes possible with the integration of focus fields [4]. In the last decade, research groups around the world designed and implemented many MPI scanners for specific applications (mouse, rat, etc.). In addition to large bore size, spatial resolution is another significant parameter that is correlated with gradient field strength (T/m) of the selection field. A gradient field strength of 7 T/m was implemented and the effect of the tracer agent core size was investigated to achieve optimum spatial resolution [5].

Fundamentally MPI technique is based on the field-free point (FFP) selection field in closed bore geometry. However,

The associate editor coordinating the review of this manuscript and approving it for publication was Hengyong Yu.

TABLE 1. Brief overview of the imaging modalities [16], [17], [18], [19], [20], [21], [22], [23], [24], [25].

Modality	Ultrasound	CT	MRI	SPECT	PET	MPI
Spatial Resolution*	1 mm	<1 mm	1 mm	3-10 mm	4 mm	< 1 mm (Preclinical)
Acquisition time*	< 1 s	1 s	10 s- 30 min	1 min	1 min	<0.1 s (preclinical)
Sensitivity*	~10-12 Molar	Millimolar	Millimolar	Picomolar	Picomolar	Micromolar (preclinical)
Quantifiability	No	Yes	No	Yes	Yes	Yes
Harmfulness	Heating and cavitation	Ionizing radiation	Heating and PNS	Ionizing radiation	Ionizing radiation	Heating and PNS
Contrast agents/tracers	Microbubbles (contrast agent)	Iodine (contrast agent)	Gadolinium, SPIO (contrast agent)	Radionuclide (radioactive tracer)	Radionuclide (radioactive tracer)	SPIO (Magnetic tracer)
Imaging method	Anatomic imaging	Anatomic imaging	Anatomic imaging	Tracer imaging	Tracer imaging	Tracer imaging

* These are widely accepted generalized values, subject to variation based on instrumentation and tracer agent specifications.

Goodwill introduced the field-free line (FFL) selection field in 2012 for MPI imaging [6]. FFL is a significant achievement that promises high sensitivity and less acquisition time as compared to FFP. Furthermore, MPI scanners of versatile methodologies such as single-sided, open bore (combination of two single-sided setups), and a traveling wave MPI scanner have been constructed in the last ten years [7], [8]. The first commercial preclinical scanner for small animal (rate, mouse) imaging was developed by Bruker Biospin MRI GmbH (FFP, 3D) with a 12 cm bore size in 2014 [9] and Magnetic Insight Inc. (FFL, 2D) with 6 cm bore size in 2017 [10]. Few research groups have focused on the implementation of a human brain size MPI scanner with medium bore size [11], [12]. The main hurdle for the transition of the MPI device from preclinical setups for small animals to a clinical machine for humans has been the lack of sufficient bore size.

MPI is not an anatomical/morphological imaging modality, so an additional imaging modality is required to recognize the exact biodistribution of the tracer material. The magnetic resonance imaging (MRI) technique was successfully integrated with classic MPI [13], [14]. However, the long acquisition time of the MRI is a disadvantage to the combined technique. On the contrary, computed tomography (CT) has the potential of simultaneous scanning with MPI. Hence hybrid CT-MPI scanner for the simultaneous acquisition was performed [15]. MPI is a tracer imaging technique like positron emission tomography (PET) and single-photon emission computed tomography (SPECT). Excellent properties of the MPI offer real-time imaging with high spatial resolution as compared to other imaging modalities as presented in Table 1.

Superparamagnetic iron oxide nanoparticles (SPIONs) are well-known based on their usage in MRI as negative contrast agents that create back holes (suppress background noise). However, SPIONs are used as positive tracer agents that become the sole signal source (hot spot) for MPI which is an emerging medical imaging technique. MPI is a non-invasive imaging technique that utilizes S-shaped (non-linear) magnetic characteristics of the SPIONs.

The MRI signals do not directly depend on SPIONs, however, The MPI signals that are only generated from SPIONs support quantifiability (signal strength linearly depends on biodistribution). Apart from instrumentation specifications, tracer agents play a crucial role in the Spatio-temporal resolution of the MPI scanners.

II. MPI TRACER AGENTS

MPI uses superparamagnetic iron oxide nanoparticles (SPIONs) as a tracer agent to carry out a scan of the objects (phantoms, in vitro, and in vivo applications). MPI exploits the nonlinear magnetization behavior of the nanoparticles to the applied magnetic field. SPIONs have a long history in medical imaging as a contrast agent in MRI [26]. Tracer and contrast agents, antibodies, magnetic hyperthermia, and drug delivery are key clinical usage of the SPIONs. They are the only source of signals in MPI, and the image is formed from the distribution of the nanoparticles. The nonlinear magnetization behavior of the tracer can be modeled with the Langevin function [27]. An oscillating magnetic field is applied to the transmit coil of the MPI system and induced magnetization is recorded by the pick-up coil of the system.

$$M_{ideal}\left(H\left(t\right)\right) = m_s c\left(\coth\left(\alpha H\left(t\right)\right) - \frac{1}{\alpha H\left(t\right)}\right) \quad (1)$$

where $\alpha = \frac{\mu_0 m_s}{k_B T}$, $m_s = \frac{\pi D_c^3 M_s}{6}$ and c is a concentration of the SPIONs, μ_0 is the permeability of free space, T is the absolute temperature, k_B is the Boltzmann constant, m_s is the magnetic moment at saturation of a single particle, D_c is the core diameter of the single-particle, and M_s (0.6 T/μ_0 for magnetite) is the saturation magnetization.

TABLE 2. Well-known magnetic nanoparticles as tracer agents for MPI imaging.

Iron Oxide/Developer	Core material	Core diameter (nm)	Coating material	Hydrodynamic diameter (nm)	Performance
Resovist[36]/BayerPharma AG	Fe_2O_4, Fe_2O_3	4.2 (Multi-core)	Carboxydextran	62	1
Ferucarbotran[37]/Meito Sangyo Co.	Fe_3O_4	3-5 (Multi-core)	Carboxydextran	45-72	1
LS-008[37]/LodeSpin Labs	Fe_3O_4	26.3 (Single-core)	PMAO-PEG	78	1
Vivotrax[33]/magnetic Insight	Fe_2O_4, Fe_2O_3	5.5 (Multi-core)	Carboxydextran	62	1
UW[38]/University of Washington	Fe_3O_4	17 (Single-core)	PMAO-PEG	86	2x
Perimag[33]/Micromod	Fe_2O_4	19 (Multi-core)	Dextran	130	2x
Nanomag[39]/Micromod	Fe_2O_4	5-15 (Multi-core)	Dextran	100	2x
SFMIOs[40]/University of California	Fe_3O_4	12.2 (Multi-core)	Organic Phase	127.3	40x
FluidMAG-D[41]/Chemicell GmbH	Fe_2O_3	n/a (Single-core)	Dextran	50	n/a
MCP3[42]/ Charité-Universitätsmedizin	Fe_2O_3	31.72 (Multi-core)	dextran	24.4 -122.4	5x

Ideally, SPIONs do not have any hysteresis which makes them perfect tracer material for imaging tasks. Remanence and coercivity do not exist in SPIONs and they are non-toxic as well [28]. The spatial resolution of the FFP-based MPI scanners is enhanced cubically with the magnetic core size of the SPIONs. Furthermore, the sensitivity of the scanners also depends on the magnetization of the tracer materials. MPI community uses versatile iron oxides among them well-known tracer agents are presented in Table 2. Relaxation behavior of the SPIONs at the excitation applied field affects the MPI signals. Many research studies utilized the change in relaxation time of the tracer agent to map the viscosity and temperature measurement of the tracer medium [29], [30]. In addition, relaxation time constants were exploited for multicolor MPI [31], [32].

Magnetic particle spectrometer (MPS) and magnetic particle relaxometer (MPR) are simplified devices of the MPI scanners and are known as zero-dimensional MPI scanners. In our previous study, we designed and implemented an MPI relaxometer at 4.6 kHz and 9.9 kHz for the evaluation of SPIONs for MPI [33]. The In-house MPI relaxometer was used to evaluate commercially available Vivotrax (Magnetic Insight, USA), Perimag (micromod, Germany), and Synomag (micromod, Germany) SPIONs for MPI biomedical applications. The effective relaxation, spatial resolution (FWHM, mT), and relative signal strength were investigated at 4.6 kHz and 9.9 kHz, respectively. Perimag showed the highest performance for spatial resolution, However, Synomag provided the highest relative signal strength. Tracer agents play a key role in the spatio-temporal resolution of the MPI. Moreover, it has the potential to be integrated with the synthesis process of magnetic nanoparticles (MNP). A quick analysis of the synthesized MNP determines the potential probes for MPI.

Magnetite (Fe_3O_4) and maghemite (γ- Fe_2O_3) are fundamental SPIONs, however, undoped and uncoated forms become causes of agglomeration that harms biocompatibility. Therefore, doping and capping usage of divalent metal ions (M = Mn, Co, Ni, etc.) enhance and protect biocompatible $M_xFe_{3-x}O_4$ SPIONs for biomedical applications. Organic and inorganic coating minimize toxicity, improve stability, and functionalize the tracer agents for targeting ligands. PEG, PEI, dextran, citric acid (CA), polyacrylic acid (PAA), albumin, gold, and chitosan are prominent coating materials for SPIONs [34]. We have developed $NiFe_2O_4$@PAA, and $NiFe_2O_4$@CA SPIONs by a hydrothermal process for MPI applications [34]. Custom designed MPI relaxometer at 9.9 kHz was utilized to investigate essential parameters for MPI. In another study, we have proposed biocompatible manganese ferrites ($MnFe_2O_4$) coated with oleate acid for MPI applications [35]. The low relaxation time of $MnFe_2O_4$ as compared to Perimag and Vivotrx motivates fast imaging with less blurring.

III. SPATIAL ENCODING

Transmit and pick-up coils of the MPI do not differentiate inductive signals from different positions. Therefore, spatially inhomogeneous static magnetic field (selection field) is applied in superposition to the alternating (sinusoidal, Square) excitation field for localization of the probes. Initially, the field free point (FFP) scheme was presented as spatial encoding, so the nanoparticles in the vicinity of the FFP generate a full MPI signal while the nanoparticles at other positions become saturated in the presence of the strong static magnetic field. Furthermore, field-free line (FFL) as shown in Figure 1 is another spatial encoding scheme that increases sensitivity, signal-to-noise ratio (SNR), and temporal resolution of the MPI scanners [43], [44].

Versatile MPI scanners based on FFP, and FFL spatial encoding were designed and implemented at the preclinical stage around the world and a few of them are presented

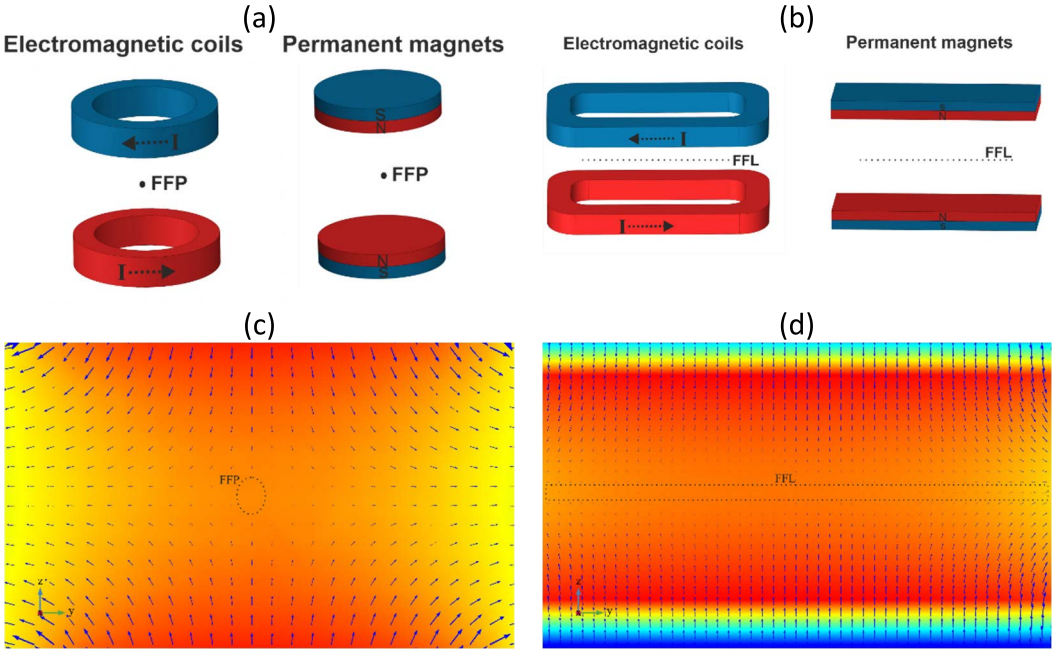

FIGURE 1. Selection fields for MPI scanners; (a) Disc-shaped permanent magnets and ring-shaped electromagnets are commonly used to generate FFP, (b) Rectangular shaped permanent magnets and electromagnets are usually used to achieve FFL, (c) Magnetic field strength pattern of FFP spatial encoding, (d) Magnetic field strength pattern of FFL spatial encoding [45].

TABLE 3. Brief overview of the magnetic particle imaging (MPI) scanners.

Institution/System	Gradient (T/m)	Bore size (mm)	FOV	Acquisition time	Tracer
Philips/Fast MPI Demonstrator[3]	5.5	32	20.4x12x16.8 mm^3	21.5 ms	Saline diluted Resovist
Philips/Fast MPI Demonstrator with enlarged FOV[52]	2.5	65 (for special coil)	34.5x24.3x17 mm^3	517 ms	Resovist
UC Berkeley/Narrowband MPI[53]	4.5	38	15x60 mm^2	10.3 min	fluidMAG-D
UC Berkeley/Narrowband MPI with stronger gradient[54]	6.5	40	3x30x20 mm^3	7 min	SPION tracer
UC Berkeley/X-space MPI[55] (mouse/rat)	7	70	55x45 mm^2	2 min	Diluted Resovist (1:2)
U Würzburg/Traveling Wave MPI[8]	4	29	65x25x25 mm^3	133 s	Fercarbotran
U Würzburg/MPI-MRI[13]	4	26	65x25 mm^2	4.35 s	Resovist
TUHH-UKE/MPI head scanner[12]	0.2	190-250	140x100 mm^2	0.5 s	Perimag
Field Free Line (FFL)					
UC Lübeck/FFL[56]	1.08	26/30	24.85x24.85 mm^2	2 min (Approximate)	Resovist
UC Berkely/FFL[57]	2.3	n/s	60x60x104 mm^3	1.3 min	Diluted Resovist
U Osaka/FFL[58]	3.2	25	24mm (circular)	20 min (Approximate)	Diluted Resovist
Aselsan/FFL-Open bore[59]	0.6	Open bore	34x18 mm^2	1 min (minimum)	Perimag
UC Berkely/FFL[60]	6.3	n/a	51.6 × 85.2 mm^2	130 min	LS-017
Commercially Available System					
Bruker/MPI-FFP[9]	2.5	119	100x100x100 mm^3	21.5 ms	n/a
Magnetic Insight Momentum/MPI-FFL[10]	6.2	60	60x60x120 mm^3		n/a

in Table 3. In our previous study, we thoroughly studied the FFP-based selection field generation with permanent magnets and electromagnets. Analytical results (MATLAB) and numerical findings (COMSOL Multiphysics) are found to be in good agreement for the 4.3 T/m gradient field [46]. Spatial homogeneity of the permanent magnets, electromagnets, and

hybrid systems was evaluated. The selection field implementation with hybrid topology was found to be 96.8% spatial homogeneous. Moreover, hybrid systems (NdFeB and electromagnets) also provide an opportunity to adjust FOV for MPI scanning.

Generally, the selection field is generated from two setups equal in magnitude but opposite in magnetic direction, so magnetic fields cancel each other at the midpoint of the geometry. Gradient field homogeneity mainly depends on the size, shape, and distance between two components of the selection field. The selection field setup is designed based on Maxwell configuration which describes optimum homogeneity distance between two centers of the selection field components as $\sqrt{3}$ R (R is the radius of each component). Gauss's law of electromagnetism defines the divergence of the selection magnetic field in 3D. The homogeneity greater than 95% would produce artifact-free images in MPI [6] otherwise wrapping artifacts around the edges of FOV will complicate image reconstruction [47]. Gradient field strength is a key parameter that characterizes spatial resolution, sensitivity, and SNR of the MPI scanner. The major challenge in scaling up the MPI technique from pre-clinical to human size is the effective implementation of the selection field. So far, permanent magnets and laminated iron core returns with electromagnets are utilized to reduce power dissipation [6].

IV. SIGNAL GENERATION AND RECEPTION

Electromagnetic coils are used as transmitters (drive coils) and pickup (receive coils) in MPI. Spatially homogeneous excitation fields are obtained from solenoid or Helmholtz configured electromagnetic coils. Generally, solenoid drive coils are utilized along the bore axis of the scanners. Saddle-shaped or fingerprint-shaped drive coils are mounted perpendicular to the bore axis. Litz wire is preferred both for drive and receive coils to mitigate the skin effect of high-frequency signals. The optimum length of the drive coils is 1.7 times their radius [48].

Drive fields have two main purposes in MPI. One, it is used to equally excite nanoparticles in the FOV region. Second, it also translates the FFP or FFL region of the MPI scanner. Each imaging axis needs to drive and receive coil pair to excite and receive nanoparticle response respectively. Excitation fields can be defined along with 3D (x, y, z) as [3]:

$$H_D(\boldsymbol{t}) = \begin{bmatrix} A_D^x Sin(2\pi f_x t) \\ A_D^y Sin(2\pi f_y t) \\ A_D^z Sin(2\pi f_z t) \end{bmatrix} \tag{2}$$

where A_D^x, A_D^y,A_D^z are amplitudes of excitation fields along x, y, and z axes, respectively. Similarly, f_x, f_y, f_z are operating frequencies along x, y, and z axes, respectively.

Superposition of the inhomogeneous selection field and homogeneous excitation fields steer the FFP inside the FOV region. The relationship among excitation frequencies ensures the trajectory pattern of the FFP. The maximum volume covered by the FFP movement can be estimated by:

$$FOV_D = \frac{4A_D^x}{G} \times \frac{4A_D^y}{G} \times \frac{2A_D^z}{G} \tag{3}$$

where G is the maximum gradient field along the z-axis (selection field components are placed along the z-axis).

FOV directly increases with the amplitude of the excitation fields. However, overheating of the patient specific absorption rate (SAR) and peripheral nerve stimulation (PNS) limit the amplitude of the excitation fields. The maximum amplitude of the excitation fields would not be greater than 10 mT for human-sized MPI scanners [49], [50], [51]. The optimum frequency of the excitation fields is 25 kHz approximately in MPI.

A large FOV is feasible with a low gradient field (G), however, spatial resolution decreases with a low G value. So, a large FOV is not possible with optimum excitation fields and gradient fields. Low-frequency focus field is applied additionally to slowly translate FFP or FFL in the FOV region. Safety limits such as PNS and SAR are ensured with the use of the focus field. The use of a low-frequency focus field introduced multi-patch FOV. Usually, drive and focus fields are obtained from a single electromagnetic coil to effectively utilized the available volume of the MPI scanners [59]. Generally, sinusoidal excitation fields are applied in MPI by all research groups around the world. However, Tay et all presented pulsed excitation field phenomena in MPI, and pulse-shaped relaxation of the tracer is thoroughly explained [61].

Generally, each imaging axis requires for receive coil to pick up tracer response. Tracer agents induce a voltage on the receive coils relying on higher harmonics of the fundamental excitation frequency. Unfortunately, inductive coupling between the drive and receive coils also induces a fundamental component which is known as the feedthrough phenomena. Direct feedthrough of the drive coil is 10^9-10^{12} times stronger than particle signal, so its existence is unacceptable. Geometric-based gradiometric modification of the receive coils cancels out 10^3-10^5 feedthrough effect on the receive coil signal. Electronic circuits like higher-order high pass and band stop filters are an alternative option for the cancellation of the feedthrough signal. Even for better cancellation, both approaches can be used together [62].

V. SIGNAL CHAIN AND IMAGING SEQUENCE

A control console is the main unit for the users to operate MPI devices. All hardware parts (selection field, drive, and receive coils) are assembled to operate from the control console. The signal flow in the MPI device is presented in Figure 2. Apart from MPI components, electronic filters have a key role in the selection and suppression of the harmonics of the MPI signal. Only a single harmonic excitation field is ensured with a higher-order band pass filter (BPF). Similarly, feedthrough cancellation is achieved with a band stop filter (BSF) to bring receive coil signal into the dynamic range of the data acquisition card (DAQ).

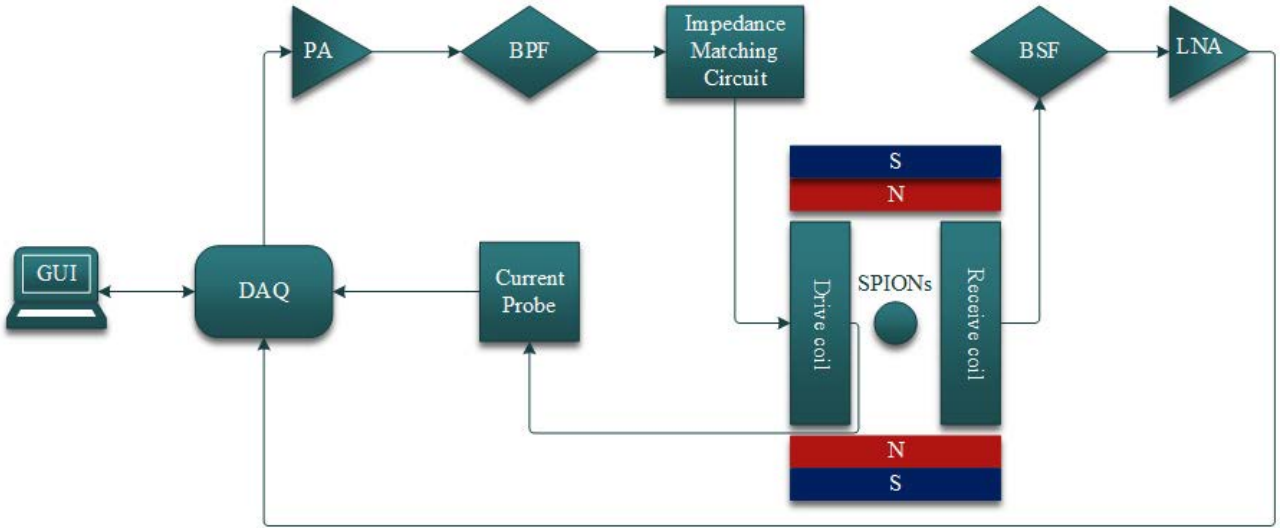

FIGURE 2. MPI device is controlled from a control console (graphical user interface, GUI) for imaging. The sinusoidal signal is generated from the data acquisition card (DAQ) and amplified with a power amplifier (PA). Unnecessary harmonics are blocked with a band pass filter (BPF) except the main operating frequency and power reduction of the drive coil are ensured with an impedance matching circuit. A selection field is generated with single pair of permanent magnets represented with north (N) and south (S) poles. Superparamagnetic iron oxide nanoparticles (SPIONs) are placed inside the field of view region of the MPI scanner. Tracer-induced signal is passed through band stop filter (BSF) to remove feedthrough signal followed by low noise amplification (LNA) of the received signal before data recording by DAQ device for post-processing [63].

The selection field setup generates a 3D gradient field for spatial encoding either on FFP or FFL pattern. However, drive and receive coils are 1D, so they are implemented for each axis separately. Mechanical movement of the test object (phantom, torso, patient) with just a single drive and receive coil can provide 3D images at the cost of acquisition time.

In MPI, an imaging sequence is classified by the movement of the FFP or FFL dynamic region. Lissajous, spiral, cartesian, radial, and bidirectional cartesian trajectories based on FFP patterns were simulated [64]. Bidirectional cartesian and Lissajous sampling patterns have proven the best spatial resolution so far [64]. However, the bidirectional cartesian trajectory is not frequently used in the implementation instead unidirectional cartesian sampling pattern. Just one drive and receive pair is enough to shift and scan all planes line-by-line. On the contrary, the Lissajous trajectory needs 2 or 3 drive and receive pairs to quickly scan the imaging volume. The minimum acquisition time of the Lissajous trajectory outperformed the other imaging sequences.

As the amplitude of the excitation fields is restricted by the PNS and SAR values, FOV (movement of FFP) does not cover all imaging volumes. Consequently, the focus field was introduced to enhance the limits of the FOV which is known as multi-patch imaging sequencing. Tracer agents outside of partial FOV contribute a signal in the receive coil due to the S-shape magnetization curve of the tracer particles [65]. This issue complicates the edge-to-edge multi-patch sequences. Over scanning of the partial FOV is an option to achieve artifacts-free images otherwise artifacts appeared at the edges of the partial FOV. However, the measurement of the over-scanning region is not trivial. An increased number of patches would increase acquisition time for large bore-size MPI devices. In addition, FFL spatial encoding reduces the need for drive-receive pairs. 3D imaging with FFL only needs two drive-receive pairs which may be implemented in either Lissajous or cartesian sampling pattern.

VI. ESSENTIAL IMAGING PARAMETERS

MPI scanners have promise for many medical applications like other imaging modalities. There are a few significant parameters that define the MPI specifications and provide an opportunity to compare it with other imaging modalities as presented in Table 1.

A. SPATIAL RESOLUTION

The most significant parameter for imaging modalities is the spatial resolution which defines how close two objects can be differentiated. The spatial resolution of the MPI scanner can be represented as [34];

$$\Delta x = \frac{k_B T}{\mu_0 m G} \Delta \varepsilon_{FWHM} \tag{4}$$

where k_B is Boltzmann constant, T is temperature, μ_0 is the magnetic permeability of the vacuum, m is the magnetic moment, $\Delta \varepsilon_{FWHM}$ is the FWHM of the PSF of the tracer agents, and β depends on the third power of the core diameter of the magnetic nanoparticles. G is the gradient of the static selection field (*FFP/FFL*). Δx describes the classical spatial resolution of the MPI scanner, it can be further increased by applying deconvolution to the MPI images. Signal-to-noise (SNR) of the acquired MPI data is also not considered. The spatial resolution of the MPI imaging modality mainly depends on the gradient field (T/m) and FWHM (mT) of the tracer obtained from PSF.

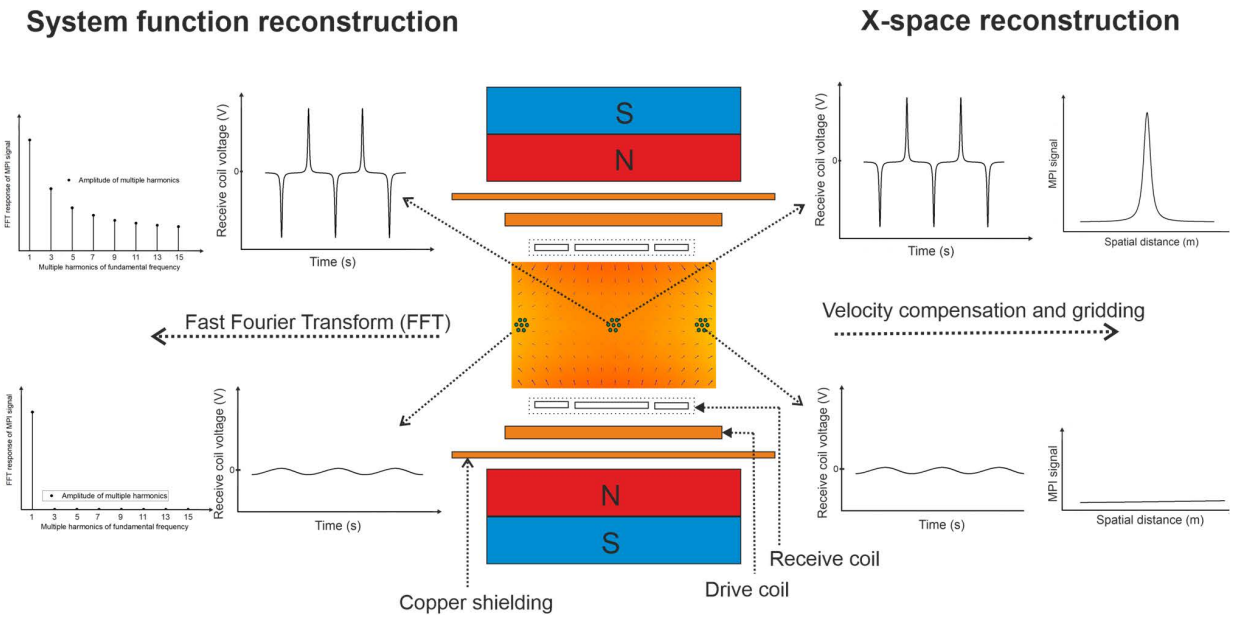

FIGURE 3. System function (frequency domain) and X-space (time-domain) are two prominent image reconstruction techniques. A simplified MPI scanner of one drive and one receive coil is displayed in the middle. N and S represent the north and south poles of the permanent magnets, respectively. Maximum MPI signal is obtained at zero field region (midpoint), however, tracer response becomes saturated at the outer edges of the FOV region [45].

B. SENSITIVITY AND TEMPORAL RESOLUTION

Temporal resolution represents the scanning time (acquisition time) of the object. Acquisition time depends on the frequency of excitation fields. While the sensitivity of the MPI scanners explores the detection of the minimum amount of tracer agents [20].

$$SNR \propto \sqrt{T}^{meas} c_0 \frac{P^R f^E}{G^3 \sqrt{R^P}} \tag{5}$$

here T^{meas} represents total measurement time and P^R is the sensitivity of the pickup coil. f^E is the excitation frequency. P^R is the noise resistance of the receive coil.

Tracer agent concentration has a linear relationship with the SNR. Similarly, the sensitivity of the receive coil also enhances the SNR of the MPI scanners linearly. The SNR also has an inverse relation with the 3rd power of the gradient field strength while the spatial resolution of the MPI scanners has a direct relation with SNR. However, gradient field strength does not enhance the spatial resolution of the scanners if the SNR of the signal is low.

C. DETECTION LIMITS

MPI utilizes radio frequencies (1-100kHz) for excitation fields and signal reception. Due to the low-frequency range coil noise dominates the body noise. It means, still there is substantial room for technical enhancement in MPI sensitivity [28].

$$\textit{Detection limits} \approx 2\rho\sqrt{k_B} \cdot \frac{NF\sqrt{T_{coil}R_{coil}}}{P^R} \cdot \frac{H_{sat}}{M_{sat}} \cdot \frac{\sqrt{BW}}{WH_{ampl}} \tag{6}$$

NF represents the noise figure of the preamplifier, k_B is the Boltzmann constant, and BW stands for final receive bandwidth.

The detection limit of the MPI scanner mainly depends on the instrumentation (hardware) parameter, nanoparticles (tracer) parameters, and scanning parameters.

VII. IMAGE RECONSTRUCTION

Direct visualization of the MPI signal is not feasible without transforming the voltage signal to particle concentrations. Image reconstruction time and image quality are trademarks of the post-processing techniques. A linear relationship between particle concentration and measured signal is the main assumption in all reconstruction techniques. Mainly two reconstruction approaches such as frequency domain-based system matrix, and time-domain based x-space are widely used for image reconstruction [66]. The signal outcomes of both approaches at two different magnetic field regions are graphically presented in Figure 3.

The system function can be measured from calibration-based, model-based, and hybrid approaches. A delta sample of the tracer agent is used and translated with a 3D actuator in a calibration-based system matrix approach [1]. It does not require any mathematical representation of the MPI hardware components or response of the tracer agent. The MPI signal (u) relation with system matric (S) is defined as.

$$Sc = u \tag{7}$$

where c is particle concentration in the FOV.

All system imperfections are considered in this approach; however, it is very time-consuming. Overall MPI system

is simulated in a model-based approach with nearly accurate sensitivity and transfer function of the receive channels [67], [68]. The exact modeling of the nanoparticle response to excitation fields is a key factor in the model-based approach as well. Meanwhile, the hybrid approach integrates both simulation and calibration aspects of the MPI scanner. 3D actuator movement was removed and the focus field for emulation of the selection field was included for a robust and accurate system matrix [69], [70], [71]. Overall, acquisition of the system matrix is tedious as compared to x-space reconstruction.

The time-domain x-space technique offers fast image reconstruction of the particle concentrations [63], [72]. Applied field homogeneity and infinite fast relaxation of the tracers are driving assumptions of the x-space technique. Receive coil voltage is normalized with FFP movement followed by the gridding of the MPI signal on the FFP scanning pattern. A simplified mathematical relation between tracer concentration (c) and recorded voltage [72] is defined by;

$$c\,(x) = \frac{u\,(x)}{\upsilon_{FFP}\,(x)} \tag{8}$$

where u(x) is the receive coil voltage at a known position inside FOV. $\upsilon_{\mathrm{FFP(x)}}$ represents the FFP velocity.

Gradiometric design of receive coils and analog filters on the receive channels remove the feedthrough effect and tracer response at the excitation frequency. Fortunately, the missing information only brings dc offset in the reconstructed signal that can be recovered with continuity boundary conditions [73], [60]. Frequency-dependent relaxation behavior of the magnetic nanoparticle delayed the receive coil voltage in comparison to the excitation field. Relaxation-based delay leads to shifting of the MPI signal in spatial mapping at the gridding stage [75]. Furthermore, the relaxation behavior of the nanoparticles can be modeled as an exponentially decaying function convolved with the magnetic nanoparticles' magnetization response [75]. A blurring in the reconstructed image can be cleaned with deconvolution techniques such as Wiener filtering.

A. DEEP LEARNING AND ARTIFICIAL INTELLIGENCE

There are many traditional image reconstruction techniques based on system matrix and x-space database proposed in the literature for MPI. However, classic methods take more time for image reconstruction which affects the acquisition time and SNR of the MPI scanner. Recently, image reconstruction based deep learning (DL), machine learning (ML), and artificial intelligence (AI) for MPI are proposed.

Deep image prior (DIP) based on a deep neural network was applied to the Open MPI dataset and results are compared with iterative regularization techniques in terms of peak signal-to-noise ratio [76]. In another study, fusing a dual-sampling convolutional neural network (FDS-MPI) was proposed to enhance spatial resolution by a factor of two and improve image quality [77].

In vivo tracking and quantification of implanted islet organoid grafts with machine learning-based K-means++ algorithm was performed [78]. The outcomes show that MPI reconstruction with ML algorithm can monitor in vivo biomedical applications and perform quantitative analysis of the tracer agents for a long duration. In another study, K-means++ based artificial intelligence (AI) model was demonstrated for pancreatic islet transplantation [79]. Islet numbers and predicted total iron values (TIV) were linearly correlated which enhances the quantification capabilities of the AI based MPI reconstruction methods. Therefore, reconstruction with AI based models will enhance the application areas of MPI. It will bring more control over monitoring test objects under observation.

VIII. APPLICATIONS OF MPI

The real-time imaging capability of the MPI technique with high temporal and spatial resolution opened the window to innovative biomedical applications. It is free of iodine-based contrast agents and does not have ionizing radiations. On the contrary, SPIONs are used as tracer agents in MPI. The quantitative nature of the MPI signal to the particle concentrations enables cell-based measurements in tissue perfusion and stenosis [63], [80]. MPI has a huge potential for a wide range of applications such as vascular and perfusion imaging, MPI-guided thermal therapy, lung imaging, oncology imaging, etc. as shown in Figure 4.

A. VASCULAR AND PERFUSION IMAGING

SPIONs are injected into a blood vessel and blood pool imaging is performed with time. The efficiency of vascular imaging depends on the magnetization response of the tracer agents and blood circulation half-time. The blood circulation time of the SPIONs is the main challenge that can be overcome by changing the chemical properties of the SPIONs [37]. Attachment of the SPIONs to the red blood cells enhances the blood circulation time, so, MPI images can be obtained after a long time (many hours) before they accumulate in the liver and spleen [81], [82]. In-vivo visualization of the living rats implanted left lower mammary tumors and right lower flank was demonstrated as shown in Figure 5. The living rats were categorized into Group A and Group B, and administered with high contrast 15 mg/kg and low contrast 5 mg/kg tracer agents, respectively. The LS-008 tracer agent coated with Polyethylene glycol (PEG) provided a stable and persistent intravascular MPI signal after many hours [83]. The signal intensity of the LS-008 is 4 times stronger than Resovist.

The MPI images were captured for $4 \times 4 \times 5.8$ cm^3 FOV in 5 min for Group A. The intensity of MPI along with time shows the initial rim enhancement (4 hr), accumulation (24 hr), and clearance (96 hr) stages of the nanoparticles as shown in Figure 5(a). In addition to this, the full body biodistribution of the tracer agent LS-008 was scanned for $4 \times 4 \times 14.5$ cm^3 in 9 min for Group B. The biodistribution dynamics of the tracer agent for the full body are visible

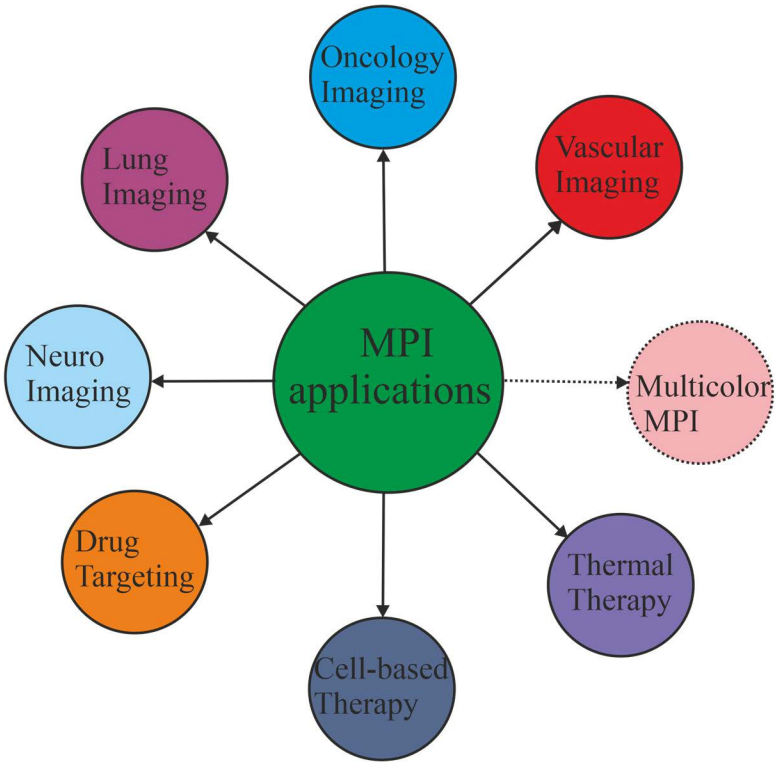

FIGURE 4. High spatial and temporal resolution of the MPI brings a revolution in the medical imaging field. MPI is at the preclinical stage and possible applications of this technique are being explored. Multicolor MPI utilizes the relaxation characteristics of the SPIONs which is a future trend [45].

as shown in Figure 5(b). The concentration for Group A is 3 times stronger than Group B and it is verified by MPI image intensities as shown in Figure 5(c) and Figure 5(d). Furthermore, the diagnosis of mild degrees of traumatic brain injuries is very challenging with CT and MRI. An experiment on a living mouse was performed to observe the clearance of the affected region as compared to healthy mice [85]. In addition to this, stoke imaging with MPI has a high potential for visualization due to cerebral perfusion. The visualization of the gastrointestinal bleeding is also possible MPI, and even precise localization of the bleeding can be determined with MPI [60].

B. MAGNETIC HYPERTHERMIA THERAPY

Magnetic hyperthermia (MHT) utilizes high frequency alternating electromagnetic field (AMF) to generate heat (elevate the temperature to 43 °C – 45 °C) with magnetic nanoparticles and kill the malignant cells around a specific region [86], [87]. Tissues at any depth are accessible with MHT without the need for invasive catheters.

MHT can easily be adopted with chemotherapy and radiotherapy-based cancer treatments. Systematically delivered magnetic nanoparticles to the targeted location accumulate in off-target organs such as the spleen and liver after some time. High magnetic field existence everywhere results in damage to these organs [88]. The challenges associated with hyperthermia are resolved by integrating with MPI hardware. Strong magnetic gradient fields of the MPI are capable to assist the MHT setup in the selection specific region. Field free region (FFR) of the MPI is shifted to the cancer cell's location followed by AMF application to increase the temperature of the target region by avoiding off-target effects [89], [90], [91]. Hyperthermia setup is integrated with an MPI scanner to diagnose bad tissues and apply treatment with high-frequency magnetic fields are presented in Figure 6. Experimental tests were performed on the U87MG xenograft mouse model. Custom design SPIONs were administered in two steps, initially 1.25 mg of Fe SPIONs by intratumoral injection followed by 50 μL of 25 mg/mL SPION through tail injection. MPI scanning (Step 1) only brings negligible heating inside the scanning region of the experimental object due to the low excitation field at low excitation field (20 kHz). However, the hyperthermia system heats the scanning region by more than 10 °C as compared to MPI scanning due to higher excitation frequency [89]. MPI images are evaluated and the affected region is marked up (Step 2) for MHT treatment. In therapy mode, initially, a gradient field is applied to isolate unhealthy regions (Step 3). Finally, the magnetic field is applied at a higher frequency (354 kHz) for the specific time interval.

In another study, a magnetically activated drug delivery system was proposed that used radio frequency alternating

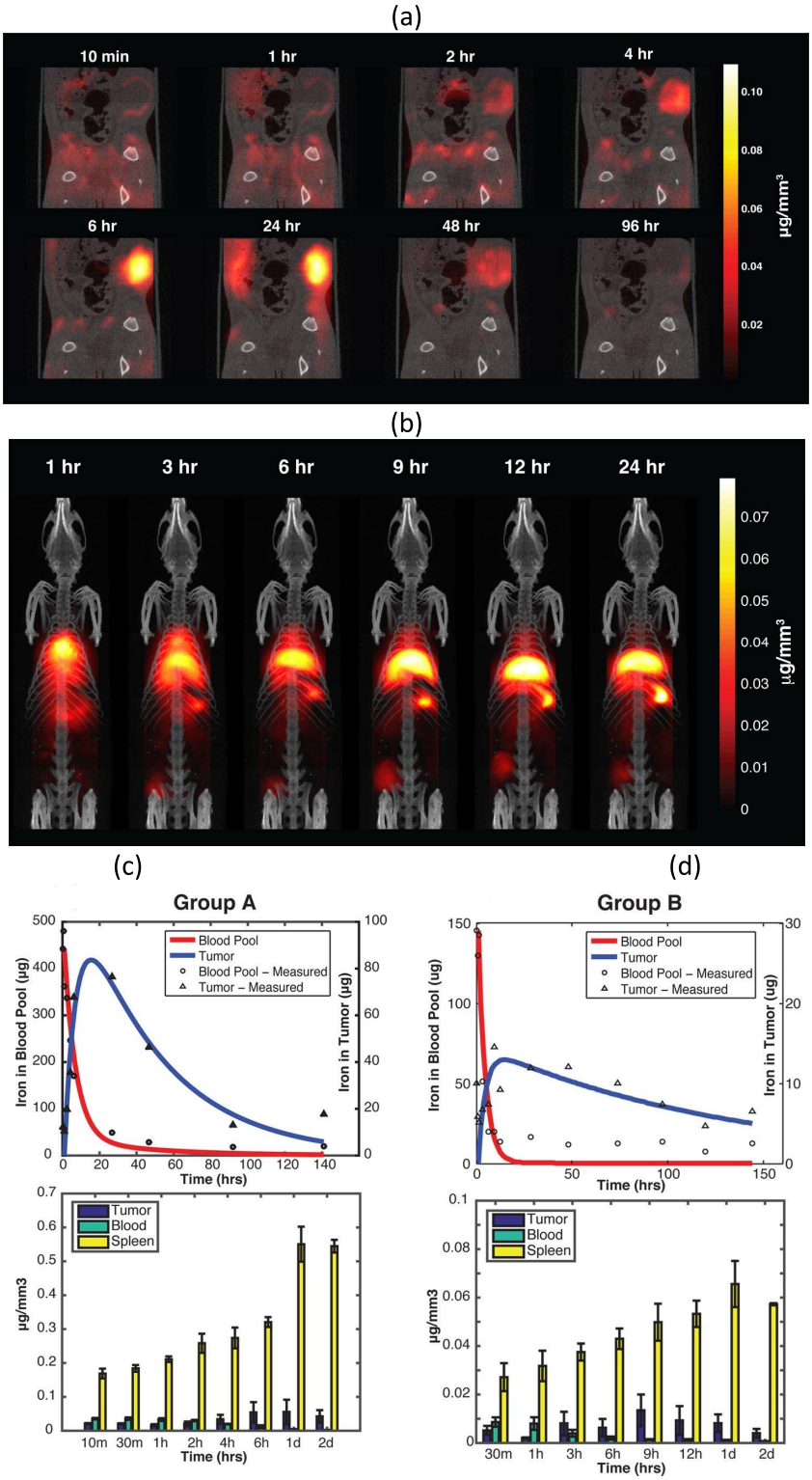

FIGURE 5. 3D MPI with a 7 T/m gradient field (FFP-based spatial encoding) was used for vascular imaging. A drive field frequency of 20.225 kHz with an excitation field strength of 40 mT_{pp}. MPI scans were integrated with CT skeletal reference. (a) The living rats (Group A) with implanted mammary tumors were scanned with an MPI scanner using a 15 mg/kg dose of LS-008 tracer agent. (b) The living rats (Group B) with implanted tumors at the right lower flank were scanned with an MPI scanner using a 5 mg/kg dose of LS-008 tracer agent. (c) Two-compartment model fitting and biodistribution for Group A. (d) Two-compartment model fitting and biodistribution for Group B. The image was adapted with permission from ACS publications [84].

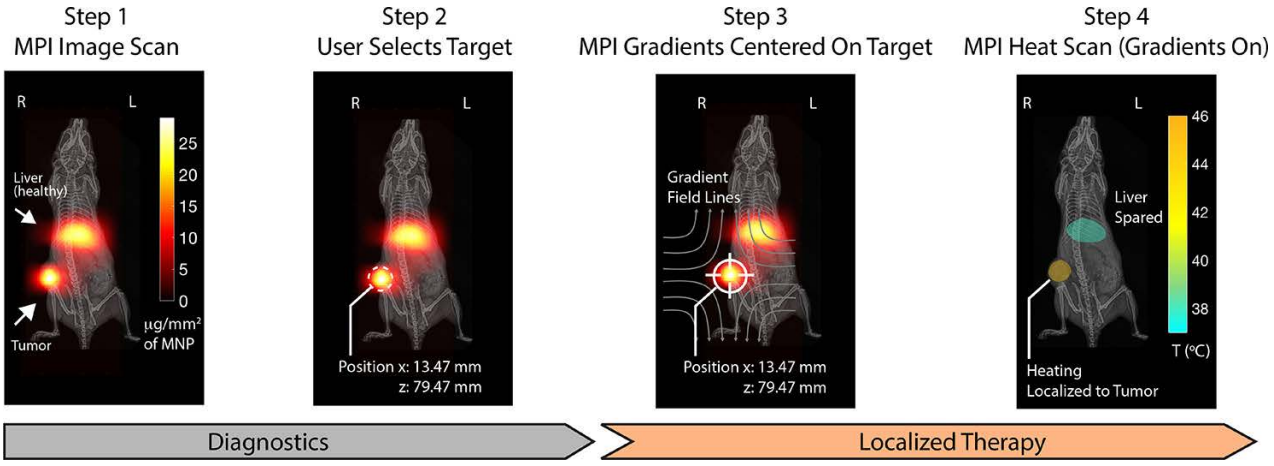

FIGURE 6. Magnetic hyperthermia therapy consists of diagnostics and therapy phases. MPI images were obtained with a 2. 35 T/m selection field (FFL) and 20 mT excitation field at 20 kHz. (Step 1) MPI images of the healthy and tumor region were overlaid to the static MRI image, (Step 2) The position of the tumor region was determined after diagnosis, (Step 3) Tumor region was localized with a gradient field to contain the heating region, (Step 4) Excitation field of 13 mT at 354 kHz were applied to generate heat with same tracer agent in the presence of gradient field. Healthy tissues were protected with a localization approach to the tumor treatment. The image was adapted with permission from ACS publications [89].

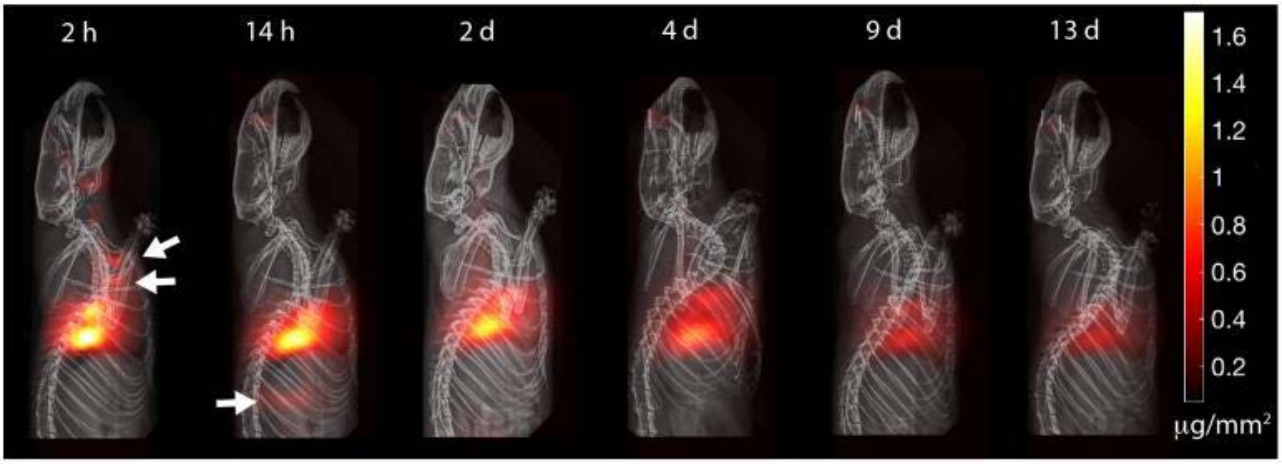

FIGURE 7. Time-based assessment of the clearance of administered aerosol. MPI scanner of 6.3 T/m gradient field strength (FFL) was used to obtain the distribution of the Perimag SPIONs (tracer agent). A magnetic field of 40 mT_{pp} was applied at 20.225 kHz excitation frequency. The clearance pathways represented with white arrows show boli in the trachea and gastrointestinal tract. MPI signals do not decay very quickly over time, so it is a suitable technique to image aerosol clearance. The gradual decay of the MPI signals over the lungs was demonstrated successfully. The image was adapted with permission from Ivy spring international publisher [95].

magnetic fields to release the drug from nanoliposomes [92]. MPI spatial encoding was applied to achieve localized target regions. Drug carriers that lie on FFP or FFL regions are susceptible to radio frequency triggered drug release.

C. LUNG IMAGING

Pulmonary drug delivery is complex due to rapid absorption. Monitoring and quantification of the aerosol is not an easy task. Existing imaging modalities like X-ray and CT rely on contrast agents for imaging human anatomy. Among other imaging techniques, PET and gamma scintigraphy have higher efficacy in aerosol imaging with picomolar sensitivity [93], [94]. However, radioactive inhaling by the patient is a major drawback and the main source of ionizing radiation risk to the lungs. MPI has a high potential to address the challenges in lung imaging. SPIONs are used as tracer agents (signal source) and mixed with aerosol to track them with MPI. The aerosol applications of MPI were demonstrated for the evaluation of delivery efficacy and tracking of the inhaled therapeutics [95] as shown in Figure 7. Perimag (micromod, Germany) SPIONs were mixed with the aerosol for in vivo tracking through MPI. The magnetic core size of the tracer agents plays a critical role to measure the MPI performance, however, biodistribution can be controlled by changing the coating (hydrodynamic) size of the magnetic nanoparticles. Perimag has a hydrodynamic size of 130 nm which restrict the blood-lung penetration. Perimag tracer agents were observed just above the lung after 2 h. However,

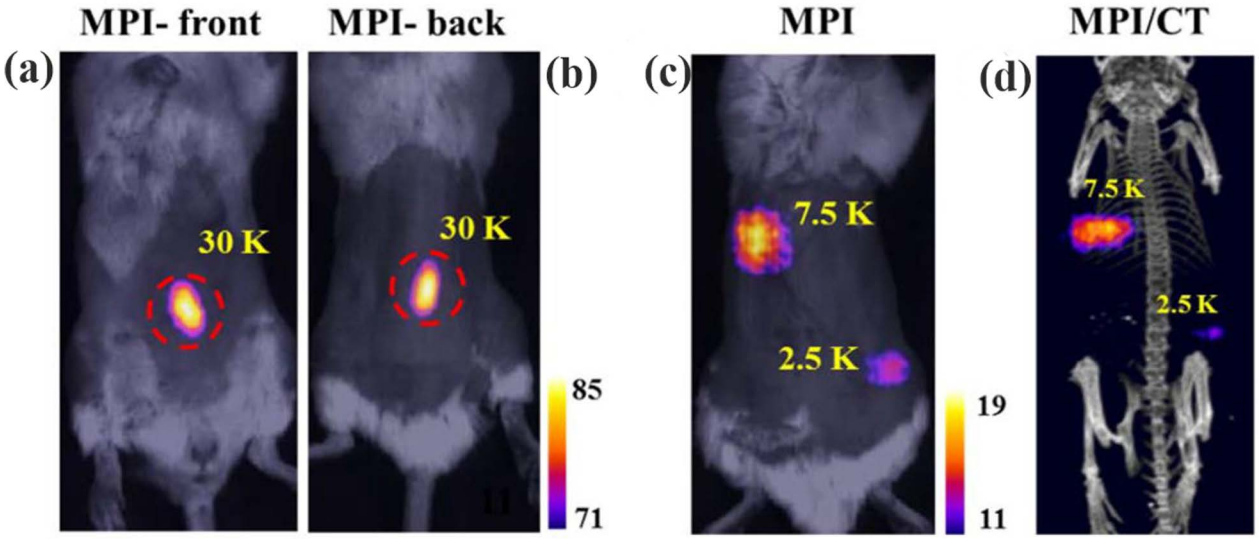

FIGURE 8. MPI images of the Fe_3O_4@PFODBT-COOH (stem cells) implanted mouse. (a) Distribution of the stem cells scanned from the front, (b) Distribution of the stem cells scanned from the back, (c) MPI image of two different locations with different stem cell concentrations, (d) 3D MPI colored images were overlaid on CT image after subcutaneous injection of functional cells. The image is reused with permission from ACS publications [101].

the tracer agents quickly moved to the lower gastrointestinal tract after 14 h. For 13 days, tracer agents (MPI signals) were gradually removed from the lung [95]. In the future, MPI can become powerful imaging and therapy technique for lung applications.

D. STEM CELL LABELING AND TRACKING

SPIONs-based MPI has gained more attention due to the high sensitivity, specificity, and quantification of the labeled cells. The sensitivity of the MPI scanners is being enhanced to detect even a single stem cell in near future. Tissue regeneration properties of the stem cell may be helpful in cardiac and neurological diseases [96]. Stem cell-based therapy has a significant potential for Parkinson's disease, Huntington's disease, amyotrophic lateral sclerosis, multiple sclerosis, Alzheimer's disease, stroke, spinal cord injury, and brain tumors [97].

MPI is a quantitative method with high sensitivity as compared to existing imaging modalities, especially MRI. Tumor-associated macrophages' presence and distribution were evaluated with MRI and MPI with the same SPIO nanoparticles [98]. Similarly, MPI and fluorine-19 MRI were utilized to measure the cellular sensitivity of breast cancer and mesenchymal stem cells (MSC) [99]. Acquisition time was kept the same for both imaging techniques for a fair comparison. MPI easily detected 4×10^3 MSC while a minimum of 256×10^3 were detected with fluorine-19 MRI.

Moreover, MPI is a safer imaging modality for monitoring intravenously human mesenchymal stem cells [100]. Mesenchymal stem cells can be used as a therapy tool for stroke, traumatic brain injury, and cancer diseases. Various experiments have been demonstrated on small animals such as rats and mice. Cell tracking with MPI was performed by implanting Fe_3O_4@PFODBT-COOH labeled HeLa cells (Janus particles) implanted into a living mouse scan with MPI, MRI, and CT imaging [101] as shown in Figure 8. A mouse with 30,000 labeled cells was visualized with 2-D projection MPI as shown in Figure 8(a).

In another study, 5×10^5 SPIO-labeled human neural progenitor cells (NPCs) were implanted in the forebrain cortex of a rat and monitored with MPI for 87 days [102]. The implanted cells remained in the object for a very long time and the clearance process was very slow which helps to monitor the object.

IX. CONCLUSION

In this study, a thorough review of MPI scanners has been accomplished. Tracer agents, spatial encoding (FFP/FFL), excitation fields and pickup systems, image reconstruction, and biomedical applications are extremely indispensable areas of the MPI technique. Technical specifications of the MPI scanners such as gradient field, bore size, excitation fields, and pulse sequences have gradually improved especially bore size since its first invention in 2005. The research on the upscaling of MPI technology is already underway. As MPI does not provide morphological structure so integration with other imaging modalities is unavoidable. Therefore, few multimodal imaging tools such as MPI-MRI and MPI-CT are also demonstrated at the pre-clinical stage. Preliminary research on MPI has achieved remarkable outcomes in various fields such as cell tracking, oncology imaging, vascular imaging, functional imaging, drug delivery, neuroimaging, and magnetic thermal therapy. The successful implementation of pre-clinical MPI scanners yielded huge expectations

from the pre-clinical (animal) to clinical (human) transition stage. Outstanding features of the MPI make it an exceptional imaging device that can play a significant role as a diagnostic, drug delivery, and monitoring tool in medical imaging. Early age cancer detection would be possible with this emerging medical imaging technique.

REFERENCES

[1] B. Gleich and J. Weizenecker, "Tomographic imaging using the nonlinear response of magnetic particles," *Nature*, vol. 435, no. 7046, pp. 1214–1217, Jun. 2005.

[2] B. Gleich, J. Weizenecker, and J. Borgert, "Experimental results on fast 2D-encoded magnetic particle imaging," *Phys. Med. Biol.*, vol. 53, no. 6, pp. N81–N84, Mar. 2008.

[3] J. Weizenecker, B. Gleich, J. Rahmer, H. Dahnke, and J. Borgert, "Three-dimensional real-time *in vivo* magnetic particle imaging," *Phys. Med. Biol.*, vol. 54, no. 5, pp. L1–L10, Mar. 2009.

[4] B. Gleich, J. Weizenecker, H. Timminger, C. Bontus, I. Schmale, J. Rahmer, J. Schmidt, J. Kanzenbach, and J. Borgert, "Fast MPI demonstrator with enlarged field of view," in *Proc. Int. Soc. Magn. Reson. Med.*, vol. 18. Stockholm, Sweden, 2010, p. 218.

[5] Z. W. Tay, D. W. Hensley, E. C. Vreeland, B. Zheng, and S. M. Conolly, "The relaxation wall: Experimental limits to improving MPI spatial resolution by increasing nanoparticle core size," *Biomed. Phys. Eng. Exp.*, vol. 3, no. 3, May 2017, Art. no. 035003.

[6] P. W. Goodwill, J. Konkle, B. Zheng, E. U. Saritas, and S. M. Conolly, "Projection x-space magnetic particle imaging," *IEEE Trans. Med. Imag.*, vol. 31, no. 5, pp. 1076–1085, May 2012.

[7] T. Sattel, T. Knopp, S. Biederer, B. Gleich, J. Weizenecker, J. Borgert, and T. Buzug, "Single-sided device for magnetic particle imaging," *J. Phys. D, Appl. Phys.*, vol. 42, no. 2, Dec. 2008, Art. no. 022001.

[8] P. Vogel, M. A. Rückert, P. Klauer, W. H. Kullmann, P. M. Jakob, and V. C. Behr, "Traveling wave magnetic particle imaging," *IEEE Trans. Med. Imag.*, vol. 33, no. 2, pp. 400–407, Feb. 2014.

[9] *Bruker Biospin MRI GmbH 2014*. Accessed: May 20, 2022. [Online]. Available: https://www.bruker.com/en/products-and-solutions/preclinical-imaging/mpi.html

[10] Magnetic Insight, Inc. (2017). *Magnetic Insight Momentum MPI Scanner*. Accessed: Jun. 6, 2022. [Online]. Available: https://www.magneticinsight.com/momentum-imager

[11] J. Rahmer, C. Stehning, and B. Gleich, "Remote magnetic actuation using a clinical scale system," *PLoS ONE*, vol. 13, no. 3, Mar. 2018, Art. no. e0193546.

[12] M. Graeser, F. Thieben, P. Szwargulski, F. Werner, N. Gdaniec, M. Boberg, F. Griese, M. Möddel, P. Ludewig, D. van de Ven, O. M. Weber, O. Woywode, B. Gleich, and T. Knopp, "Human-sized magnetic particle imaging for brain applications," *Nature Commun.*, vol. 10, no. 1, pp. 1–9, Apr. 2019.

[13] P. Vogel, S. Lother, M. A. Ruckert, W. H. Kullmann, P. M. Jakob, F. Fidler, and V. C. Behr, "MRI meets MPI: A bimodal MPI-MRI tomograph," *IEEE Trans. Med. Imag.*, vol. 33, no. 10, pp. 1954–1959, Oct. 2014.

[14] J. Franke, U. Heinen, H. Lehr, A. Weber, F. Jaspard, W. Ruhm, M. Heidenreich, and V. Schulz, "System characterization of a highly integrated preclinical hybrid MPI-MRI scanner," *IEEE Trans. Med. Imag.*, vol. 35, no. 9, pp. 1993–2004, Sep. 2016.

[15] P. Vogel, J. Markert, M. A. Rückert, S. Herz, B. Keßler, K. Dremel, D. Althoff, M. Weber, T. M. Buzug, T. A. Bley, W. H. Kullmann, R. Hanke, S. Zabler, and V. C. Behr, "Magnetic particle imaging meets computed tomography: First simultaneous imaging," *Sci. Rep.*, vol. 9, no. 1, pp. 1–9, Sep. 2019.

[16] T. F. Massoud and S. S. Gambhir, "Molecular imaging in living subjects: Seeing fundamental biological processes in a new light," *Genes Develop.*, vol. 17, pp. 545–580, Mar. 2003.

[17] M. H. Pablico-Lansigan, S. F. Situ, and A. C. S. Samia, "Magnetic particle imaging: Advancements and perspectives for real-time *in vivo* monitoring and image-guided therapy," *Nanoscale*, vol. 5, no. 10, p. 4040, 2013.

[18] A. Meola, J. Rao, N. Chaudhary, G. Song, X. Zheng, and S. D. Chang, "Magnetic particle imaging in neurosurgery," *World Neurosurg.*, vol. 125, May 2019, Art. no. 2610270.

[19] T. Knopp and T. M. Buzug, *Magnetic Particle Imaging: An Introduction to Imaging Principles and Scanner Instrumentation*. Heidelberg, Germany: Springer, 2012.

[20] J. Weizenecker, J. Borgert, and B. Gleich, "A simulation study on the resolution and sensitivity of magnetic particle imaging," *Phys. Med. Biol.*, vol. 52, no. 21, pp. 6363–6374, Oct. 2007.

[21] A. R. Kherlopian, T. Song, Q. Duan, M. A. Neimark, M. J. Po, J. K. Gohagan, and A. F. Laine, "A review of imaging techniques for systems biology," *BMC Syst. Biol.*, vol. 2, no. 1, p. 74, Aug. 2008.

[22] R. Weissleder, "Scaling down imaging: Molecular mapping of cancer in mice," *Nature Rev. Cancer*, vol. 2, no. 1, pp. 11–18, Jan. 2002.

[23] B. Cox and P. Beard, "Super-resolution ultrasound," *Nature*, vol. 527, no. 7579, pp. 451–452, Nov. 2015.

[24] P. W. Goodwill, E. U. Saritas, L. R. Croft, T. N. Kim, K. Krishnan, D. V. Schaffer, and S. M. Conolly, "X-space MPI: Magnetic nanoparticles for safe medical imaging," *Adv. Mater.*, vol. 24, pp. 3870–3877, Mar. 2012.

[25] L. C. Wu, Y. Zhang, G. Steinberg, H. Qu, S. Huang, M. Cheng, T. Bliss, F. Du, J. Rao, G. Song, L. Pisani, T. Doyle, S. Conolly, K. Krishnan, G. Grant, and M. Wintermark, "A review of magnetic particle imaging and perspectives on neuroimaging," *Amer. J. Neuroradiol.*, vol. 40, pp. 206–212, Feb. 2009.

[26] J. Dulińska-Litewka, A. Łazarczyk, P. Hałubiec, O. Szafrański, K. Karnas, and A. Karewicz, "Superparamagnetic iron oxide nanoparticles—Current and prospective medical applications," *Materials*, vol. 12, no. 4, p. 617, Feb. 2019.

[27] S. Chikazumi and S. H. Charap, *Physics of Magnetism*. Malabar, FL, USA: Krieger, 1978.

[28] P. Chandrasekharan, Z. W. Tay, X. Y. Zhou, E. Yu, R. Orendorff, D. Hensley, Q. Huynh, K. L. B. Fung, C. C. VanHook, P. Goodwill, B. Zheng, and S. Conolly, "A perspective on a rapid and radiation-free tracer imaging modality, magnetic particle imaging, with promise for clinical translation," *Brit. J. Radiol.*, vol. 91, no. 1091, Nov. 2018, Art. no. 20180326.

[29] M. Utkur, Y. Muslu, and E. U. Saritas, "Relaxation-based viscosity mapping for magnetic particle imaging," *Phys. Med. Biol.*, vol. 62, pp. 3422–3439, May 2017.

[30] J. B. Weaver, A. M. Rauwerdink, and E. W. Hansen, "Magnetic nanoparticle temperature estimation," *Med. Phys.*, vol. 36, pp. 1822–1829, May 2009.

[31] J. Rahmer, D. Wirtz, C. Bontus, J. Borgert, and B. Gleich, "Interactive magnetic catheter steering with 3-D real-time feedback using multi-color magnetic particle imaging," *IEEE Trans. Med. Imag.*, vol. 36, no. 7, pp. 1449–1456, Jul. 2017.

[32] Y. Muslu, M. Utkur, O. B. Demirel, and E. U. Saritas, "Calibration-free relaxation-based multi-color magnetic particle imaging," *IEEE Trans. Med. Imag.*, vol. 37, no. 8, pp. 1920–1931, Jan. 2018.

[33] M. Irfan, N. Dogan, T. Sapmaz, and A. Bingolbali, "Development of MPI relaxometer for characterization of superparamagnetic nanoparticles," *J. Magn. Magn. Mater.*, vol. 536, Oct. 2021, Art. no. 168082.

[34] M. Irfan, N. Dogan, A. Bingolbali, and F. Aliew, "Synthesis and characterization of $NiFe_2O_4$ magnetic nanoparticles with different coating materials for magnetic particle imaging (MPI)," *J. Magn. Magn. Mater.*, vol. 537, Nov. 2021, Art. no. 168150.

[35] N. Dogan, O. M. Dogan, M. Irfan, F. Ozel, A. S. Kamzin, V. G. Semenov, and I. V. Buryanenko, "Manganese doped-iron oxide nanoparticles and their potential as tracer agents for magnetic particle imaging (MPI)," *J. Magn. Magn. Mater.*, vol. 561, Nov. 2022, Art. no. 169654.

[36] P. Reimer and T. Balzer, "Ferucarbotran (Resovist): A new clinically approved RES-specific contrast agent for contrast-enhanced MRI of the liver: Properties, clinical development, and applications," *Eur. Radiol.*, vol. 13, no. 6, pp. 1266–1276, Jun. 2003.

[37] P. Keselman, Y. Y. Elaine, X. Y. Zhou, P. W. Goodwill, P. Chandrasekharan, R. M. Ferguson, and A. P. Khandhar, "Tracking short-term biodistribution and long-term clearance of SPIO tracers in magnetic particle imaging," *Phys. Med. Biol.*, vol. 62, pp. 3440–3453, May 2017.

[38] A. P. Khandhar, R. M. Ferguson, H. Arami, and K. M. Krishnan, "Monodisperse magnetite nanoparticle tracers for *in vivo* magnetic particle imaging," *Biomaterials*, vol. 34, no. 15, pp. 3837–3845, May 2013.

[39] D. Eberbeck, C. L. Dennis, N. F. Huls, K. L. Krycka, C. Gruttner, and F. Westphal, "Multicore magnetic nanoparticles for magnetic particle imaging," *IEEE Trans. Magn.*, vol. 49, no. 1, pp. 269–274, Jan. 2013.

[40] Z. W. Tay, S. Savliwala, D. W. Hensley, K. L. B. Fung, C. Colson, B. D. Fellows, X. Zhou, Q. Huynh, Y. Lu, B. Zheng, P. Chandrasekharan, S. M. Rivera-Jimenez, C. M. Rinaldi-Ramos, and S. M. Conolly, "Superferromagnetic nanoparticles enable order-of-magnitude resolution & sensitivity gain in magnetic particle imaging," *Small Methods*, vol. 5, no. 11, Nov. 2021, Art. no. 2100796.

[41] L. M. Bauer, D. W. Hensley, B. Zheng, Z. W. Tay, P. W. Goodwill, M. A. Griswold, and S. M. Conolly, "Eddy current-shielded x-space relaxometer for sensitive magnetic nanoparticle characterization," *Rev. Sci. Instrum.*, vol. 87, pp. 1–7, May 2016.

[42] H. Kratz, A. Mohtashamdolatshahi, D. Eberbeck, O. Kosch, R. Hauptmann, F. Wiekhorst, M. Taupitz, B. Hamm, and J. Schnorr, "MPI phantom study with a high-performing multicore tracer made by coprecipitation," *Nanomaterials*, vol. 9, no. 10, p. 1466, Oct. 2019.

[43] J. Weizenecker, B. Gleich, and J. Borgert, "Magnetic particle imaging using a field free line," *J. Phys. D, Appl. Phys.*, vol. 41, no. 10, May 2008, Art. no. 105009.

[44] M. Erbe, T. Knopp, T. F. Sattel, S. Biederer, and T. M. Buzug, "Experimental generation of an arbitrarily rotated field-free line for the use in magnetic particle imaging," *Med. Phys.*, vol. 38, pp. 5200–5207, Sep. 2011.

[45] M. Irfan, "Design and implementation of magnetic particle imaging (MPI) scanner for medical applications," Ph.D. dissertation, Dept. Electron. Eng., Gebze Tech. Univ., Gebze, Türkiye, 2021.

[46] M. Irfan, O. M. Dogan, N. Dogan, and A. Bingolbali, "Selection field generation using permanent magnets and electromagnets for a magnetic particle imaging scanner," *Alexandria Eng. J.*, vol. 61, no. 10, pp. 7685–7696, Oct. 2022.

[47] E. Yagiz, A. R. Cagil, and E. U. Saritas, "Non-ideal selection field induced artifacts in x-space MPI," *Int. J. Magn. Part. Imag.*, vol. 6, pp. 1–9, Jun. 2020.

[48] M. Graeser, T. Knopp, P. Szwargulski, T. Friedrich, A. von Gladiss, M. Kaul, K. M. Krishnan, H. Ittrich, G. Adam, and T. M. Buzug, "Towards picogram detection of superparamagnetic iron-oxide particles using a gradiometric receive coil," *Sci. Rep.*, vol. 7, no. 1, p. 6872, Jul. 2017.

[49] E. U. Saritas, P. W. Goodwill, G. Z. Zhang, and S. M. Conolly, "Magnetostimulation limits in magnetic particle imaging," *IEEE Trans. Med. Imag.*, vol. 32, no. 9, pp. 1600–1610, Sep. 2013.

[50] E. U. Saritas, P. W. Goodwill, and S. M. Conolly, "Effects of pulse duration on magnetostimulation thresholds," *Med. Phys.*, vol. 42, no. 6, pp. 3005–3012, Jun. 2015.

[51] I. Schmale, B. Gleich, J. Schmidt, J. Rahmer, C. Bontus, R. Eckart, and B. David, "Human PNS and SAR study in the frequency range from 24 to 162 kHz," in *Proc. Int. Workshop Magn. Part. Imag. (IWMPI)*, Berkeley, CA, USA, Jun. 2013, p. 1.

[52] J. Rahmer, B. Gleich, C. Bontus, I. Schmale, J. Schmidt, J. Kanzenbach, O. Woywode, J. Weizenecker, and J. Borgert, "Rapid 3D *in vivo* magnetic particle imaging with a large field of view," in *Proc. Int. Soc. Magn. Reson. Med. (ISMRM)*, Montreal, QC, Canada, 2011, p. 3285.

[53] P. W. Goodwill, G. C. Scott, P. P. Stang, and S. M. Conolly, "Narrowband magnetic particle imaging," *IEEE Trans. Med. Imag.*, vol. 28, no. 8, pp. 1231–1237, Aug. 2009.

[54] P. W. Goodwill, P. Scott, P. Stang, G. C. Lee, D. Morris, and S. Conolly, "Direct imaging of SPIOs in mice using magnetic particle imaging: Instrument construction and 3D imaging," in *Proc. Int. Soc. Magn. Reson. Med. (ISMRM)*, Honolulu, HI, USA, 2009, p. 596.

[55] P. W. Goodwill, L. R. Croft, J. J. Konkle, K. Lu, E. U. Saritas, B. Zheng, and S. M. Conolly, "A 7 T/M 3D x-space MPI mouse and rat scanner," in *Proc. Int. Workshop Magn. Part. Imag. (IWMPI)*, Berkeley, CA, USA, Mar. 2013, p. 1.

[56] K. Bente, M. Weber, and M. Graeser, "Two dimensional magnetic particle imaging with a dynamic field free line scanner," in *Proc. 4th Int. Workshop Magn. Part. Imag. (IWMPI)*, Berlin, Germany, 2014, p. 66.

[57] J. J. Konkle, P. W. Goodwill, E. U. Saritas, B. Zheng, K. Lu, and S. M. Conolly, "Twenty-fold acceleration of 3D projection reconstruction MPI," *Biomed. Eng.*, vol. 58, no. 6, pp. 565–576, 2013.

[58] K. Murase, S. Hiratsuka, R. Song, and Y. Takeuchi, "Development of a system for magnetic particle imaging using neodymium magnets and gradiometer," *Jpn. J. Appl. Phys.*, vol. 53, no. 6, May 2014, Art. no. 067001.

[59] C. B. Top and A. Güngör, "Tomographic field free line magnetic particle imaging with an open-sided scanner configuration," *IEEE Trans. Med. Imag.*, vol. 39, no. 12, pp. 4164–4173, Dec. 2020.

[60] E. Y. Yu, P. Chandrasekharan, R. Berzon, Z. W. Tay, X. Y. Zhou, A. P. Khandhar, and R. M. Ferguson, "Magnetic particle imaging for highly sensitive, quantitative, and safe *in vivo* gut bleed detection in a murine model," *ACS Nano*, vol. 11, pp. 12067–12076, Dec. 2017.

[61] Z. W. Tay, D. Hensley, J. Ma, P. C. Sekharan, B. Zheng, P. Goodwill, and S. Conolly, "Pulsed excitation in magnetic particle imaging," *IEEE Trans. Med. Imag.*, vol. 38, no. 10, pp. 2389–2399, Oct. 2019.

[62] M. Graeser, T. Knopp, M. Grüttner, T. F. Sattel, and T. M. Buzug, "Analog receive signal processing for magnetic particle imaging," *Med. Phys.*, vol. 40, no. 4, Apr. 2013, Art. no. 042303.

[63] M. Irfan, N. Dogan, O. M. Dogan, and A. Bingolbali, "Development of magnetic particle imaging (MPI) scanner for phantom imaging of tracer agents," *IEEE Trans. Magn.*, vol. 58, no. 8, pp. 1–6, Aug. 2022.

[64] T. Knopp, S. Biederer, T. Sattel, J. Weizenecker, B. Gleich, J. Borgert, and T. Buzug, "Trajectory analysis for magnetic particle imaging," *Phys. Med. Biol.*, vol. 54, pp. 385–397, Jan. 2009.

[65] A. Weber, F. Werner, J. Weizenecker, T. M. Buzug, and T. Knopp, "Artifact free reconstruction with the system matrix approach by overscanning the field-free-point trajectory in magnetic particle imaging," *Phys. Med. Biol.*, vol. 61, pp. 475–487, Jan. 2016.

[66] M. Grüttner, T. Knopp, J. Franke, M. Heidenreich, J. Rahmer, A. Halkola, C. Kaethner, J. Borgert, and T. M. Buzug, "On the formulation of the image reconstruction problem in magnetic particle imaging," *Biomed. Eng.*, vol. 58, no. 6, pp. 583–591, Jan. 2013.

[67] T. Knopp, T. F. Sattel, S. Biederer, J. Rahmer, J. Weizenecker, B. Gleich, J. Borgert, and T. M. Buzug, "Model-based reconstruction for magnetic particle imaging," *IEEE Trans. Med. Imag.*, vol. 29, no. 1, pp. 12–18, Jan. 2010.

[68] T. Knopp, S. Biederer, T. F. Sattel, J. Rahmer, J. Weizenecker, B. Gleich, J. Borgert, and T. M. Buzug, "2D model-based reconstruction for magnetic particle imaging," *Med. Phys.*, vol. 37, pp. 485–491, Feb. 2010.

[69] M. Graeser, S. Biederer, M. Grüttner, H. Wojtczyk, W. Tenner, T. F. Sattel, B. Gleich, J. Borgert, and T. M. Buzug, "Determination of a 1D-MPI-system-function using a magnetic particle spectroscope," in *Biomedical Technology* (Deutsche Gesellschaft für Biomedizinische Technik Jahrestagung), vol. 56, Berlin, Germany, 2011.

[70] M. Gruettner, M. Graeser, S. Biederer, T. F. Sattel, H. Wojtczyk, W. Tenner, T. Knopp, B. Gleich, J. Borgert, and T. M. Buzug, "1D-image reconstruction for magnetic particle imaging using a hybrid system function," in *Proc. IEEE Nucl. Sci. Symp. Conf. Rec.*, Valencia, Spain, Oct. 2011, pp. 2545–2548.

[71] A. Halkola, T. M. Buzug, J. Rahmer, B. Gleich, and C. Bontus, "System calibration unit for magnetic particle imaging: Focus field based system function," in *Magnetic Particle Imaging* (Springer Proceedings in Physics), vol. 140, T. Buzug, J. Borgert, Eds. Berlin, Germany: Springer, 2012.

[72] P. W. Goodwill and S. M. Conolly, "Multidimensional x-space magnetic particle imaging," *IEEE Trans. Med. Imag.*, vol. 30, no. 9, pp. 1581–1590, Sep. 2011.

[73] P. Lu, P. Goodwill, B. Zheng, and S. Conolly, "The impact of filtering direct-feedthrough on the x-space theory of magnetic particle imaging," *Proc. SPIE*, vol. 7965, Mar. 2011, Art. no. 79652I.

[74] K. Lu, P. W. Goodwill, E. U. Saritas, B. Zheng, and S. M. Conolly, "Linearity and shift invariance for quantitative magnetic particle imaging," *IEEE Trans. Med. Imag.*, vol. 32, no. 9, pp. 1565–1575, Sep. 2013.

[75] L. R. Croft, P. W. Goodwill, and S. M. Conolly, "Relaxation in x-space magnetic particle imaging," *IEEE Trans. Med. Imag.*, vol. 31, no. 12, pp. 2335–2342, Sep. 2012.

[76] S. Dittmer, T. Kluth, M. T. R. Henriksen, and P. Maass, "Deep image prior for 3D magnetic particle imaging: A quantitative comparison of regularization techniques on open MPI dataset," 2007, *arXiv:2007.01593*.

[77] Y. Shang, J. Liu, L. Zhang, X. Wu, P. Zhang, L. Yin, H. Hui, and J. Tian, "Deep learning for improving the spatial resolution of magnetic particle imaging," *Phys. Med. Biol.*, vol. 67, no. 12, Jun. 2022, Art. no. 125012.

[78] A. Sun, H. Hayat, S. Liu, E. Tull, J. O. Bishop, B. F. Dwan, M. Gudi, N. Talebloo, J. R. Dizon, W. Li, J. Gaudet, A. Alessio, A. Aguirre, and P. Wang, "3D *in vivo* magnetic particle imaging of human stem cell-derived islet organoid transplantation using a machine learning algorithm," *Frontiers Cell Develop. Biol.*, vol. 9, Aug. 2021, Art. no. 704483.

[79] H. Hayat, A. Sun, H. Hayat, S. Liu, N. Talebloo, C. Pinger, J. O. Bishop, M. Gudi, B. F. Dwan, X. Ma, Y. Zhao, A. Moore, and P. Wang, "Artificial intelligence analysis of magnetic particle imaging for islet transplantation in a mouse model," *Mol. Imag. Biol.*, vol. 23, no. 1, pp. 18–29, Feb. 2021.

[80] J. Haegele, J. Rahmer, R. Duschka, C. Schaecke, N. Panagiotopoulos, J. Tonak, J. Borgert, J. Barkhausen, and F. M. Vogt, "Magnetic particle imaging (MPI): Visualization and quantification of vascular stenosis phantoms," in *Proc. 4th Int. Workshop Magn. Part. Imag. (IWMPI)*, Berlin, Germany, Dec. 2014, pp. 57–58.
[81] A. Antonelli, C. Sfara, J. Rahmer, B. Gleich, J. Borgert, and M. Magnani, "Red blood cells as carriers in magnetic particle imaging," *Biomed. Eng.*, vol. 58, no. 6, pp. 517–525, Jan. 2013.
[82] J. Rahmer, A. Antonelli, C. Sfara, B. Tiemann, B. Gleich, M. Magnani, J. Weizenecker, and J. Borgert, "Nanoparticle encapsulation in red blood cells enables blood-pool magnetic particle imaging hours after injection," *Phys. Med. Biol.*, vol. 58, pp. 3965–3977, Jun. 2013.
[83] A. P. Khandhar, P. Keselman, S. J. Kemp, R. M. Ferguson, P. W. Goodwill, S. Conolly, and K. M. Krishnan, "Evaluation of PEG-coated iron oxide nanoparticles as blood pool tracers for preclinical magnetic particle imaging," *Nanoscale*, vol. 9, pp. 1299–1306, Jan. 2017.
[84] E. Y. Yu, M. Bishop, B. Zheng, R. M. Ferguson, A. P. Khandhar, S. J. Kemp, K. M. Krishnan, P. W. Goodwill, and S. M. Conolly, "Magnetic particle imaging: A novel *in vivo* imaging platform for cancer detection," *Nano Lett.*, vol. 17, no. 3, pp. 1648–1654, Mar. 2017.
[85] R. Orendorff, A. J. Peck, B. Zheng, S. N. Shirazi, R. M. Ferguson, A. P. Khandhar, and S. J. Kemp, "First *in vivo* traumatic brain injury imaging via magnetic particle imaging," *Phys. Med. Biol.*, vol. 62, pp. 3501–3509, May 2017.
[86] A. Chicheł, J. Skowronek, M. Kubaszewska, and M. Kanikowski, "Hyperthermia—Description of a method and a review of clinical applications," *Rep. Practical Oncol. Radiotherapy*, vol. 12, no. 5, pp. 267–275, Sep. 2007.
[87] E. A. Périgo, G. Hemery, O. Sandre, D. Ortega, E. Garaio, F. Plazaola, and F. J. Teran, "Fundamentals and advances in magnetic hyperthermia," *Appl. Phys. Rev.*, vol. 2, no. 4, Dec. 2015, Art. no. 041302.
[88] C. Kut, Y. Zhang, M. Hedayati, H. Zhou, C. Cornejo, D. Bordelon, J. Mihalic, M. Wabler, E. Burghardt, C. Gruettner, A. Geyh, C. Brayton, T. L. Deweese, and R. Ivkov, "Preliminary study of injury from heating systemically delivered, nontargeted dextran–superparamagnetic iron oxide nanoparticles in mice," *Nanomedicine*, vol. 7, no. 11, pp. 1697–1711, Nov. 2012.
[89] Z. W. Tay, P. Chandrasekharan, A. Chiu-Lam, D. W. Hensley, R. Dhavalikar, X. Y. Zhou, E. Y. Yu, P. W. Goodwill, B. Zheng, C. Rinaldi, and S. M. Conolly, "Magnetic particle imaging-guided heating *in vivo* using gradient fields for arbitrary localization of magnetic hyperthermia therapy," *ACS Nano*, vol. 12, no. 4, pp. 3699–3713, Mar. 2018.
[90] D. Hensley, Z. W. Tay, R. Dhavalikar, B. Zheng, P. Goodwill, C. Rinaldi, and S. Conolly, "Combining magnetic particle imaging and magnetic fluid hyperthermia in a theranostic platform," *Phys. Med. Biol.*, vol. 62, no. 9, pp. 3483–3500, Apr. 2017.
[91] T. Kuboyabu, M. Yamawaki, M. Aoki, A. Ohki, and K. J. I. J. N. N. Murase, "Quantitative evaluation of tumor early response to magnetic hyperthermia combined with vascular disrupting therapy using magnetic particle imaging," *Int. J. Nanomed. Nanosurg.*, vol. 2, no. 3, pp. 1–7, 2016.
[92] J. F. Liu, N. Neel, P. Dang, M. Lamb, J. McKenna, L. Rodgers, B. Litt, Z. Cheng, A. Tsourkas, and D. Issadore, "Radiofrequency-triggered drug release from nanoliposomes with millimeter-scale resolution using a superimposed static gating field," *Small*, vol. 14, no. 44, Nov. 2018, Art. no. 1802563.
[93] S. P. Newman, "Lung distribution of inhaled drugs," *Brit. J. Clin. Pharmacol.*, vol. 52, pp. 716–719, Dec. 2001.
[94] M. Dolovich, "Imaging drug delivery and drug responses in the lung," *Proc. Amer. Thoracic Soc.*, vol. 1, no. 4, pp. 329–337, Dec. 2004.
[95] Z. W. Tay, P. Chandrasekharan, X. Y. Zhou, E. Yu, B. Zheng, and S. Conolly, "*In vivo* tracking and quantification of inhaled aerosol using magnetic particle imaging towards inhaled therapeutic monitoring," *Theranostics*, vol. 8, no. 13, pp. 3676–3687, 2018.
[96] R. Sun, X. Li, M. Liu, Y. Zeng, S. Chen, and P. Zhang, "Advances in stem cell therapy for cardiovascular disease," *Int. J. Mol. Med.*, vol. 38, no. 1, pp. 23–29, Jul. 2016.
[97] S. U. Kim and J. de Vellis, "Stem cell-based cell therapy in neurological diseases: A review," *J. Neurosci. Res.*, vol. 87, no. 10, pp. 2183–2200, Aug. 2009.
[98] A. V. Makela, J. M. Gaudet, M. A. Schott, O. C. Sehl, C. H. Contag, and P. J. Foster, "Magnetic particle imaging of macrophages associated with cancer: Filling the voids left by iron-based magnetic resonance imaging," *Mol. Imag. Biol.*, vol. 22, pp. 958–968, Jan. 2020.
[99] O. C. Sehl and P. J. Foster, "The sensitivity of magnetic particle imaging and fluorine-19 magnetic resonance imaging for cell tracking," *Sci. Rep.*, vol. 11, no. 1, p. 22198, Nov. 2021.
[100] B. Zheng, M. P. von See, E. Yu, B. Gunel, K. Lu, T. Vazin, D. V. Schaffer, P. W. Goodwill, and S. M. Conolly, "Quantitative magnetic particle imaging monitors the transplantation, biodistribution, and clearance of stem cells *in vivo*," *Theranostics*, vol. 6, no. 3, pp. 291–301, Jan. 2016.
[101] G. Song, M. Chen, Y. Zhang, L. Cui, H. Qu, X. Zheng, M. Wintermark, Z. Liu, and J. Rao, "Janus iron oxides @ semiconducting polymer nanoparticle tracer for cell tracking by magnetic particle imaging," *Nano Lett.*, vol. 18, no. 1, pp. 182–189, Jan. 2018.
[102] B. Zheng, T. Vazin, P. W. Goodwill, A. Conway, A. Verma, E. U. Saritas, D. Schaffer, and S. M. Conolly, "Magnetic particle imaging tracks the long-term fate of *in vivo* neural cell implants with high image contrast," *Sci. Rep.*, vol. 5, no. 1, p. 14055, Sep. 2015.

MUHAMMAD IRFAN (Member, IEEE) received the Ph.D. degree in electronics engineering from Gebze Technical University, Türkiye, in 2021. He is currently working as a Postdoctoral Researcher with Gebze Technical University. His research has been published in several reputed international journals. His research interests include medical imaging, magnetic particle imaging (MPI) scanners, magnetic resonance imaging (MRI), localized magnetic hyperthermia, and superparamagnetic iron oxide nanoparticles (SPIONs) as tracer agent for MPI.

NURCAN DOGAN received the Ph.D. degree in physics from Gebze Technical University, Türkiye, in 2012. She is currently working as an Associate Professor with the Gebze Technical University. Her research has been published in many reputed international journals. Her research interests include medical imaging, magnetic particle imaging (MPI) scanners, magnetic resonance imaging (MRI), localized magnetic hyperthermia, and synthesis of tracer agents for MPI and MRI applications.